FEATURE ARTICLE

Check for updates

Recent advances in transition metal sulfide-based electrode materials for supercapacitors

Mengkang Zhu,[a] Dan Wang, (ID) *[a] Zongyu Ge,[a] Lin Pan,[a] Yanli Chen,[a] Wenchang Wang,[ab] Naotoshi Mitsuzaki,[c] Shuyong Jia[d] and Zhidong Chen (ID) *[a]

Supercapacitors, as highly promising charge storage systems, have attracted much attention due to their fast charging and discharging rates, high power density, and longer service life. However, compared to rechargeable batteries, the low energy density of supercapacitors limits their practical applications. Rational design of advanced electrode materials shows great potential to address the above issue. In recent years, transition metal sulfides (TMSs) have become a promising material for hybrid supercapacitors due to their low cost, excellent redox reversibility, and electronic conductivity. This comprehensive review summarizes the recent progress in synthetic methods of transition metal sulfides. Additionally, the improvement strategies for the electrochemical performance of TMSs are highlighted. Finally, the challenges and perspectives of TMSs for supercapacitors in the future are discussed.

1. Introduction

With the rapid industrialization, environmental pollution and energy scarcity have become increasingly prominent. The demand for sustainable clean energy sources, including wind, solar, and biofuels, is rising exponentially.[1–3] However, these sources are highly dependent on natural conditions.

Consequently, developing efficient energy storage systems is critical for addressing global energy demands.[4,5] Over the past few decades, rechargeable batteries and supercapacitors (SCs) have gained traction as energy storage solutions in hybrid electric vehicles, portable electronics, and industrial power systems.[6–8] While SCs offer high-power density, rapid charge/discharge rates, and long cycle life, their low energy density remains a significant limitation.[9–13] SCs are generally categorized into symmetric and asymmetric types (ASCs), based on electrode material differences. By utilizing electrodes with differing potential windows, ASCs can extend the device's operational voltage range during charging and discharging. According to the energy storage formula $E = 0.5\ CV^2$, ASCs typically exhibit higher energy density than symmetric SCs. Notably, ASCs achieve significantly greater energy density than

[a] *Jiangsu Key Laboratory of Advanced Catalytic Materials and Technology, Advanced Catalysis and Green Manufacturing Collaborative Innovation Center, School of Petrochemical Engineering, Changzhou University, Changzhou, Jiangsu, 213164, P. R. China. E-mail: danwang@cczu.edu.cn, zdchen@cczu.edu.cn*

[b] *Electrolytic Copper Foil Engineering Technology Center of Changzhou University, Changzhou, 213164, Jiangsu, P. R. China*

[c] *Qualtec Co., Ltd, Osaka, 590-0906, Japan*

[d] *Lite-on OPTO Tech (CZ) Co., Ltd, Changzhou, 213166, Jiangsu, China*

Dan Wang is currently a lecturer at the School of Petrochemical Engineering, Changzhou University, China. She received her PhD degree in 2021 from Harbin Institute of Technology, China. Her main research interests include non-precious metal-based catalysts for applications in electrocatalysis and metal–air batteries, and advanced electrode materials for super-capacitors.

Dan Wang

Zhidong Chen is currently a professor at the School of Petrochemical Engineering, Changzhou University, China. He received his PhD degree in 2000 from Yamaguchi University, Japan. His interests focus on electrocatalysis, advanced materials for batteries and capacitors, electrodeposition of functional materials, and electroanalytical chemistry.

Zhidong Chen

conventional batteries or fuel cells, while maintaining their inherent advantages in power density and cycling stability.[14,15] As a result, ASCs hold broad application prospects in future energy systems.[16–19]

Electrode materials can be categorized into three main types: metal compounds, carbon materials, and conductive polymers. Among metal compounds, TMSs are of particular interest due to their ability to undergo faradaic redox reactions (a hallmark of pseudocapacitance), which enable high theoretical specific capacitances.[20–22] Hu et al.[23] synthesized urchin-like Co–NiS$_2$/C composites with sulfur vacancies via coprecipitation and sulfidation. Benefiting from the enhanced conductivity, the optimized electrode retained 89.2% of its capacity after 8000 cycles. Ni et al.[24] fabricated Co$_3$S$_4$@NiCo$_2$S$_4$ microspheres with a core–shell structure. Their unique architecture and synthesis method endow them with excellent performance, reaching a high specific capacitance of 2697.7 F g^{-1} at 1 A g^{-1}. The most extensively studied TM-based materials include sulfides, phosphides, hydroxides, and oxides. TMSs and their composites have emerged as promising candidates for ASCs due to their high specific capacity, improved conductivity, and optimal electrochemical activity.[25–29] However, TMSs still face critical challenges including intrinsic low electrical conductivity, limited active sites, and suboptimal cycling stability.[30–32] Recently, although numerous synthesis methods and performance enhancement strategies for TMSs have been developed, a comprehensive summary and review of their intrinsic interconnections remain lacking.

In this review, the classification and energy storage mechanism of supercapacitors are firstly introduced. Then, the synthesis strategies for preparation of advanced TMS-based electrodes are summarized and compared with the highlight of the morphology. Meanwhile, the electrochemical performance of TMSs is improved by different methods, including elemental doping, introduction of sulfur vacancies, and recombination with carbon materials, which have been comprehensively discussed. Finally, the research progress of TMSs in supercapacitor electrode materials is summarized and prospected (Fig. 1).

2. Supercapacitors

SCs fundamentally comprise three main parts: electrode, electrolyte and current collector. The electrochemical performance of supercapacitors is predominantly determined by electrode materials. Notably, high capacitance can be achieved by using porous materials that can effectively increase the interfaces between the electrode surface and the electrolyte. Moreover, the porous electrode also allows more charge to accumulate or adsorb on the electrode, thereby greatly increasing the capacitance of the supercapacitor and making supercapacitors exhibit higher energy density than conventional capacitors while retaining high power density.[33–35] Noteworthily, the morphology, size and porosity can determine the specific surface area of the electrode material. Hierarchical morphologies (e.g., spherical, flower-like) with multi-scale pores enhance ion accessibility, while dense structures (e.g., cubic) may
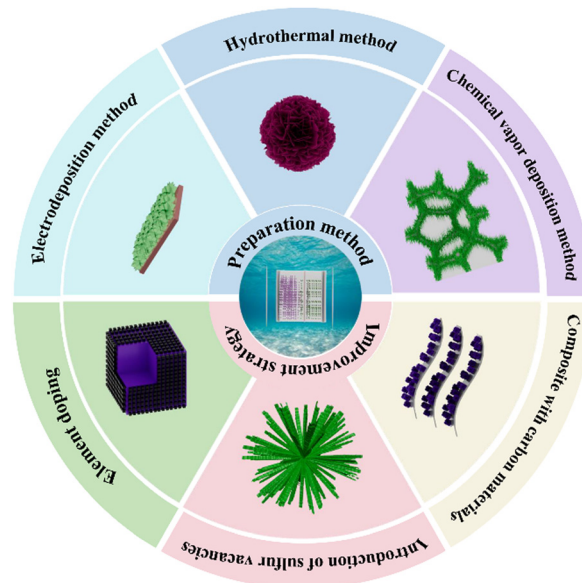

Fig. 1 Overview of the topics covered in this review.

limit electrolyte penetration, directly affecting capacitance. The pore size also influences capacitance performance. Chmiola et al.[36] revealed that microporous carbon materials with pore sizes smaller than 1 nm exhibit an anomalous increase in capacitance. This finding highlights the complex interplay between pore geometry and electrochemical performance, indicating that nanoscale pore engineering plays a crucial role in capacitance optimization. According to the energy storage mechanisms, SCs can be divided into electric double-layer capacitors (EDLCs), pseudocapacitors (PCs) and hybrid supercapacitors (HSCs).[37,38] The three types of SCs will be discussed in detail as follows (Fig. 2).

2.1. Electric double-layer capacitors

EDLCs do not undergo chemical reactions at the electrodes. The operation of EDLCs is through a non-Faraday process, which accumulates a double layer of charge at the electrode–electrolyte interface by applying a voltage to the electrode.[8,39,40] This accumulation of the double layer of charge is mainly caused by electrostatic phenomena. The reason why EDLCs can show excellent cycle stability is mainly due to the absence of redox reaction during the charge and discharge process and its high reversibility, which also reduces the rate of performance degradation of EDLCs and the volume change.[41] Compared with traditional supercapacitors, EDLCs rely on a larger
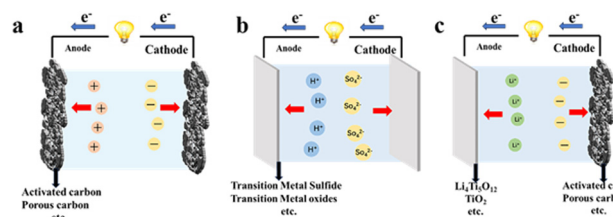

Fig. 2 Schematic diagram of the energy storage mechanisms of (a) EDLCs, (b) PCs, and (c) HSCs.

specific surface area and smaller electrode spacing, enabling higher power density (not energy density) due to rapid charge/discharge kinetics.[42,43] Generally, EDLCs commonly use aqueous electrolytes such as KOH, H_2SO_4, or neutral salts (e.g., Na_2SO_4). The electrolyte provides positive and negative ions, and the transport of these ions in the EDLCs is mainly affected by several factors, such as the wettability of the solution to the pore surface, the affinity of the tortuous mass-transfer path, the electrical phenomena associated with the solution, and the area limitation within the pore surface of the electrode.[11]

2.2. Pseudocapacitors

PCs store energy via reversible faradaic redox reactions on/near the electrode surface, distinct from irreversible battery-type reactions on electrode surfaces and electrolytes. In a reversible process, no new chemicals are formed, whereas in an irreversible Faraday process, new chemical components will be generated. PCs are stored in the same way as EDLCs, when an external voltage is applied to the PCs, the charged atoms or ions in the electrolyte will move towards the electrode with the opposite charge.[44–46] As a result, an electric double layer will form at the interface between the electrode and the electrolyte, and the charged atoms or ions within the double layer will lose electrons to the electrode surface, which will therefore be charged.[47–49] The charge transfer mechanism in the Faraday reaction depends mainly on the applied voltage, so performance of PCs is determined by the voltage. In general, the electrochemical process in PCs can be divided into three types, which are the doping and de-doping of the electrode material, the redox reaction of electrolyte ions, and the surface adsorption of ions in the electrolyte on the electrode. The first chemical process mainly relies on surface processes, so the surface space of electrode materials has no significant effect on the capacitance of PCs. However, these processes are surface-controlled, thus the performance of PCs strongly depends on the electrode's specific surface area. Normally, the preferred electrode materials for PCs are conductive polymers, metal oxides, and carbon-based materials, all of which have large specific surface areas.[50,51]

By triggering redox reactions on the electrode surface, the capacitance of PCs is many times higher than that of EDLCs.[52] However, compared with EDLCs, PCs still have some shortcomings in performance, e.g. the contraction and expansion of the electrode material caused by mechanical stress during the charging and discharging process, which will result in the insufficient cycle life and unsatisfying mechanical stability of PCs.[53,54]

2.3. Hybrid supercapacitors

Given the insufficient energy density and power density of EDLCs and PCs, hybrid supercapacitors (HSCs) have emerged and attracted attention as a new generation of energy storage devices.[55,56]

Hybrid supercapacitors (HSCs) integrate battery-type electrodes (e.g., lithium-intercalation materials) with capacitive electrodes (EDLCs or PCs) or combine EDLC materials with PC materials, enabling them to exhibit both high energy density and high-power density. Operating with asymmetric electrode configurations, HSCs are also termed asymmetric supercapacitors (ASCs). This structural asymmetry enables ASCs to achieve a wider voltage window. Since the energy stored in supercapacitors is proportional to capacitance and the square of the operating voltage, ASCs can deliver significantly higher energy densities than pure EDLCs or PCs. Meanwhile, this unique architecture effectively mitigates the drawbacks of individuals making ASCs more suitable for practical energy storage applications.[57–59]

For example, Li et al.[60] reported an ASC using MoS_2/$NiCo_2S_4$@C hollow microspheres (HMSs) as the positive electrode and activated carbon as the negative electrode. This device achieved a high energy density of 36.46 W h kg^{-1} at an ultrahigh power density of 73.75 kW kg^{-1}, maintaining 90.1% capacity retention after 10 000 charge–discharge cycles at 10 A g^{-1}. Sun et al.[61] reported another ASC with Co_9S_8@$NiCo_2S_4$ as the positive electrode and activated carbon as the negative electrode, demonstrating an impressive energy density of 58 W h kg^{-1} at a power density of 800 W kg^{-1}, along with 92.9% capacity retention after 10 000 cycles. Each type of SC has unique characteristics, and the hybrid structure based on EDLCs and PCs following asymmetric assembly offers a method to integrate two storage principles, thus positioning ASCs as versatile energy storage devices for broad applications.

3. Synthesis strategy

In recent years, compared with transition metal oxides, TMSs have good electrical conductivity, which is mainly due to the fact that the lower electronegativity of sulfur compared to oxygen weakens the metal–chalcogen bond strength, promoting structural flexibility and enhanced ion diffusion kinetics in TMS, and the electron transfer is more rapid, which greatly improves the electrochemical performance of the materia.[62–64] At the same time, TMSs are also superior to other materials in terms of mechanical stability.[65,66] Of course, TMSs also have problems such as large volume changes and slow reaction kinetics.[67] These problems can be improved by choosing different preparation methods, and the three commonly used preparation methods are hydrothermal, electrodeposition, and chemical vapor deposition. In this section, we focus on the use of these three methods to improve the morphology of materials, so as to improve the existing problems of transition metal dichalcogenides and improve the electrochemical performance of TMSs.

3.1. Hydrothermal method

The hydrothermal method mainly refers to the process of dissolving and recrystallizing insoluble reactants in water in a closed space under certain temperature and pressure conditions. It is noteworthy that different temperatures and reaction times in hydrothermal processes have a significant impact on the morphology of transition metal sulfides. Therefore, selecting appropriate hydrothermal reaction conditions is crucial for improving morphology and enhancing performance. Wang et al.[68] systematically investigated the morphological evolution

of NiCo₂S₄ by varying hydrothermal reaction times. As the reaction time increased, the tips of NiCoS nanorods became progressively rougher, resembling budding flower structures. After hydrothermal treatment for 4 h, the diameter of the nanorods stabilized, and the flower-like architecture became more distinct. Extending the reaction time to 5 h caused the "buds" at the nanorod tips to fully "bloom", resulting in narrower nanorods. Notably, the NiCoS sample prepared by 4 h exhibited the largest specific surface area due to its optimized morphology, exposing more electrochemical active sites and enabling superior electrochemical performance. Galvanostatic charge–discharge (GCD) curves revealed that the specific capacitance was 2096 F g⁻¹ by 3 h, 3093 F g⁻¹ by 4 h, and 1878 F g⁻¹ by 5 h. In addition, Gou et al.[69] found that the NiCoS sample contained abundant nanospheres after hydrothermal treatment for 1 h, and the nanospheres gradually disintegrated into nanoparticles as the reaction time increased. The sample prepared in 14 h exhibited a porous, fluffy structure with only trace residual nanospheres. After 18 h, the spherical structure nearly disappeared, indicating the critical role of reaction time in morphology regulation. BET surface area analysis showed that the sample prepared in 14 h exhibited a specific surface area of 29.9 m² g⁻¹, significantly higher than 27.9 m² g⁻¹ (10 h) and 19.6 m² g⁻¹ (18 h). Remarkably, the optimal electrode delivered excellent electrochemical stability, retaining 68.0% of its initial capacitance after 4000 cycles.

The hydrothermal temperature can also affect the final morphology and electrochemical performance. It was found that the particle size of NiS/Ni₃S₄ composites could be regulated by hydrothermal temperature.[70] At 160 °C and 180 °C, the average particle sizes were 820.9 nm and 620 nm, respectively. When the temperature was increased to 200 °C, the average particle size was greatly reduced to 290.1 nm. Notably, its superior rate capability was confirmed by retaining 56.0% of the specific capacitance at 2 A g⁻¹ when the current density increased to 20 A g⁻¹, compared to those of 43.7% (160 °C) and 49.4% (180 °C). Impressively, it achieved specific capacitances of 194.4 mA h g⁻¹ at 2 A g⁻¹ and 133.1 mA h g⁻¹ at 10 A g⁻¹, along with excellent cycling stability (89.5 mA h g⁻¹ retained after 5000 cycles at 10 A g⁻¹).

The precursor concentration is also a key factor in tailoring the morphology. Moorthi et al.[71] synthesized $Mo_{1-x}V_xS_2$ via a one-step hydrothermal method. By adjusting the Mo:V ratio, the morphology of $Mo_{1-x}V_xS_2$ transitioned from pure MoS₂ nanosheets into hierarchical flower-like microspheres. When the Mo:V ratio was 1:1, the material exhibited well-defined microspheres composed of interconnected petal-like nanosheets, featuring a smooth surface and a porous thin-layer structure. This unique structural configuration significantly increased the specific surface area and the number of electrolyte-accessible sites, resulting in superior electrochemical performance. Notably, a supercapacitor assembled using this material achieved an energy density of 19.5 W h kg⁻¹ and a maximum power density of 900 W kg⁻¹. After 10 000 charge–discharge cycles, the capacitance retention rate remained 86.3%. Mian Muhammad Faisal et al.[72] found that increasing the concentration of Na₂S precursor caused severe particle agglomeration, reducing the specific surface area

and potentially impairing the electrochemical storage capacity. The electrode prepared with 0.4 mmol of Na₂S exhibited optimal performance due to its uniform morphology, achieving a specific capacitance of 2696.2 F g⁻¹, higher than those of 998.7 F g⁻¹ (0.2 mmol) and 1911.5 F g⁻¹ (0.6 mmol). The assembled device demonstrated a high capacity of 420.10 C g⁻¹, a maximum energy density of 75.96 W h kg⁻¹, a power density of 2865 W kg⁻¹, and outstanding cycling stability (85% capacitance retention after 5000 cycles).

Moreover, hydrothermal methods can construct unique morphology and structure. Ni et al.[73] successfully transformed ZIF-67 templates into Ni–Co–Mn ternary sulfide double-layered nanoporous cages through ion exchange and hydrothermal methods. As shown in Fig. 3(a), the outer layer of these hollow cages consists of mixed metal sulfides, while the inner layer is composed of cobalt sulfide. Notably, the surface of the hollow cages features a nanosheet architecture, which not only provides abundant active sites and shortens ion/electron transport pathways during electrochemical processes but also mitigates volume expansion of the electrode material during prolonged cycling, thereby significantly enhancing its cyclic stability. Through precise structural and compositional optimization, the composite exhibits a remarkable specific capacitance of 2460 F g⁻¹ at 1 A g⁻¹, while maintaining 80.8% of its initial capacitance after 5000 charge–discharge cycles. Yang et al.[74] developed a facile hydrothermal strategy to synthesize ultrafine nickel–molybdenum sulfide ((Ni,Mo)S₂/G) enriched with active
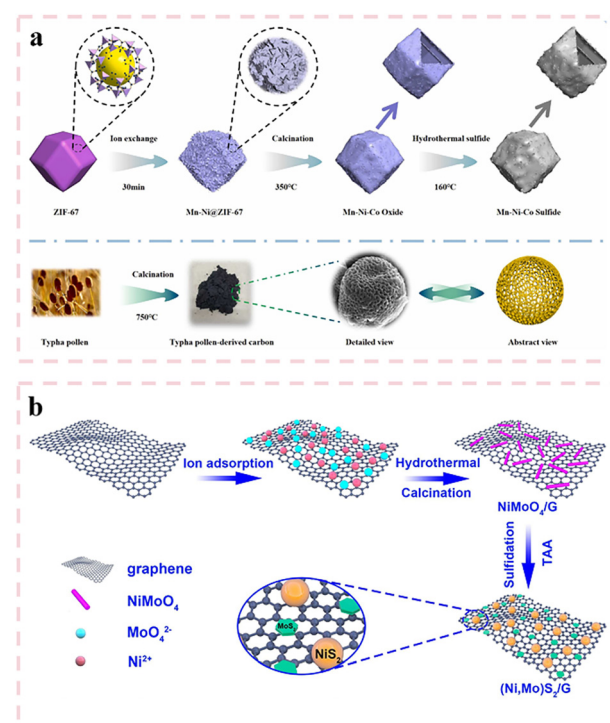

Fig. 3 (a) Schematic of cathode NMCS and anode TPC preparation processes. Reproduced with permission from ref. 73. (b) Schematic illustration of the formation process of (Ni,Mo)S₂/G via a two-step solvothermal approach. Reproduced with permission from ref. 74.

edge sites anchored on graphene nanosheets. As shown in Fig. 3(b), the $(Ni,Mo)S_2$ phase comprises a heterogeneous mixture of NiS_2 nanoparticles and MoS_2 nanosheets. The abundant active sites inherent in the $(Ni,Mo)S_2$ nanosheets, combined with the synergistic effects between $(Ni,Mo)S_2$ and graphene, synergistically accelerate faradaic redox reactions, thereby improving both rate capability and specific capacity. The optimized $(Ni,Mo)S_2$/G composite demonstrates a high specific capacitance of 2379 F g^{-1} at 1 A g^{-1}. This enhanced electrochemical performance underscores the effectiveness of the designed heterostructure in facilitating charge transfer kinetics and structural stability.

3.2. Electrodeposition method

Electrodeposition relies on applying a controlled overpotential to drive the reduction of metal ions at the electrode surface to obtain the required metal components, which is influenced by both ion concentration and redox thermodynamics. The electrodeposition method mainly changes the morphology of electrode materials by adjusting different parameters such as current density, deposition time, deposition cycle, and adding surfactants. As shown in Fig. 4(a), in 2019, Wang et al.[75] fabricated Ni_3S_2 nanosheets on carbon nanotubes (CNTs) via electrodeposition, subsequently introducing an outer CNT layer through dip-coating and drying processes, followed by crystallization of Ni_3S_2 nanoparticles via annealing treatment. The inner CNT layer electrodeposited with Ni_3S_2 nanoparticles significantly enhanced active site density, while the outer highly conductive CNT network served as efficient pathways for rapid electron transport, collectively endowing the material with exceptional electrochemical performance. The CNT–Ni_3S_2–CNT composite electrode demonstrated a remarkable areal capacitance of 13 400 mF cm^{-2} at 10 mA cm^{-2}, coupled with outstanding cycling stability—retaining 90.6% of its initial capacity after 10 000 charge–discharge cycles As shown in Fig. 4(b), in 2020, Ma et al.[76] obtained $CoMoS_4$@NiCoS nanotube hybrid arrays with layered core–shell

hollow structures through different electrodeposition cycles. When the deposition period was 6 cycles, the hollow $CoMoS_4$ nanotubes were not uniformly covered by NiCoS nanosheets, therefore it could not provide porous channels for electrolyte permeation or sufficient active sites. When the deposition period was 10 cycles, the electrode material was tightly wrapped by overly dense nanosheets, resulting in uneven arrangement and self-aggregation of the nanosheets on the hollow $CoMoS_4$ nanotubes. This also greatly suppressed the contact between the electrolyte and the electrode, leading to a decrease in electrochemical performance. When the deposition period was 8 cycles, the hollow $CoMoS_4$ nanotubes were tightly wrapped by NiCoS nanosheets, providing sufficient pores for adjacent core–shell nanotube arrays, as well as porous structure and abundant electrochemical active sites for electrolyte permeation. The 3D stacking $CoMoS_4$@ NiCoS electrode achieved a specific capacitance of 2208.5 F g^{-1} at a current density of 1 A g^{-1}, along with excellent cycling stability. The capacitance retention rate is as high as 91.3% after 5000 cycles at 3 A g^{-1}. In addition, the assembled $CoMoS_4$@NiCoS//AC ASC also exhibited excellent electrochemical performance, providing an energy density of 49.1 W h kg^{-1} at a high-power density of 800 W kg^{-1}. Meanwhile, it also exhibited excellent cycling stability, maintaining an initial capacity of 90.3% even after 10 000 cycles.

As shown in Fig. 4(c), in 2021, Pu et al.[77] synthesized the hierarchical coral-like architecture of Ni nickel cobalt hydroxysulfide nanosheet arrays (NiCo–SOH) featuring interconnected macropores and mesopores, facilitating rapid ion diffusion, through a one-step electrodeposition strategy. This hierarchical coral-like architecture features abundant surface micropores that facilitate both electron transfer and electrolyte diffusion, thereby optimizing electrochemical kinetics. The NiCo–SOH exhibited a high specific capacitance of 2092 F g^{-1} at 1 A g^{-1}, along with superior rate capability—maintaining 1696 F g^{-1} even at an elevated current density of 10 A g^{-1}. This performance enhancement stems from the synergistic combination of

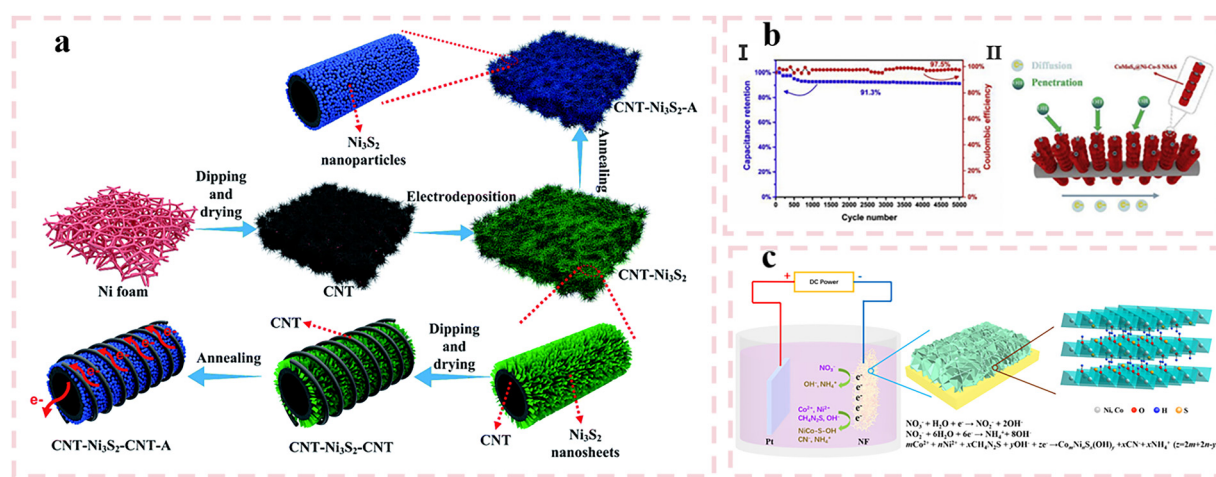Fig. 4 (a) Schematic representation of the preparation process of binder-free 3D-networked CNT–Ni_3S_2–CNT-A supported by Ni foam. Reproduced with permission from ref. 75. (b) (I) Cycling performance of the CMS-8 electrode. (II) Schematic illustration of the hierarchical core–shell hollow. Reproduced with permission from ref. 76. (c) Sketch diagram of the synthesized procedure of hydroxysulfide. Reproduced with permission from ref. 77.

hierarchical porosity and intrinsic redox activity inherent to the ternary metal composition.

At the same time, the addition of surfactants can also regulate the morphology of electrode materials. In 2023, Amala Georg et al.[78] changed the morphology of the electrode material by adding hexadecyltrimethylammonium bromide (CTAB). The addition of CTAB reduced the aggregation of $CuCo_2S_4$ nuclei, thereby promoting the uniform distribution of particles on the surface. Meanwhile, during the annealing process, CTAB decomposed into carbonaceous residues and gaseous products (e.g., CO_2, NH_3), creating a porous network and exposing additional active sites, thereby improving the electrochemical performance of the material. The $CuCo_2S_4$ nanotubes achieved a high specific capacity of 1199 C g^{-1} at a current density of 10 A g^{-1}. Even when the current density was up to 30 A g^{-1}, $CuCo_2S_4$ metal nanotubes still have an initial capacity of 83.17% after 5000 charging and discharging cycles. At the same time, the ASC also exhibited excellent performance with a specific capacity of 360.27 C g^{-1} at a current of 10 A g^{-1}. Remarkably, it retained 95.23% of capacity value after more than 5000 cycles at a current density of 30 A g^{-1}.

3.3. Chemical vapor deposition method

As one of the earlier methods used in material deposition, chemical vapor deposition refers to the process of using gaseous or vapor substances to react at the gas–solid interface and generate solid deposits on the substrate. The chemical vapor deposition (CVD) method can deposit a wide variety of sediment types, usually resulting in high purity and dense structure. The deposition process can be controlled by adjusting the deposition parameters. Zhao et al.[79] prepared a carbon cloth loaded $NiPS_3$ nanosheet array using the chemical vapor deposition method. The SEM images showed that the surface of each carbon cloth fiber was uniformly covered with dense nanostructures, which is also conducive to the electrochemical performance of the material. The $NiPS_3$ electrode delivered a high specific capacitance of 1148 F g^{-1} at a current density of 1 A g^{-1}. Meanwhile, the cycling stability of $NiPS_3$ was tested under a current density of 10 A g^{-1}, and it still maintained a capacitance retention of 81.4% after 5000 cycles. The ASC assembled by $NiPS_3$ also displayed a specific capacitance of 61.3 F g^{-1} at a current density of 1 A g^{-1} and an energy density of 19.2 W h kg^{-1} at a power density of 750 W kg^{-1}. As shown in Fig. 5(a) and (b), A. Raza et al.[80] synthesized molybdenum disulfide (MoS_2) and heterostructured magnesium sulfide (MgS)/MoS_2 nanocomposites on nickel foam via a chemical vapor deposition (CVD) method. The CVD-derived composite exhibits a high specific surface area of 170 m^2 g^{-1}, which not only exposes abundant electrochemically active sites but also enhances electrolyte–electrode interfacial contact, thereby endowing the material with exceptional electrochemical performance. The assembled supercapacitor demonstrates remarkable cycling stability, retaining 95% of its initial specific capacitance (Csp) after 10 000 charge–discharge cycles at a high current density of 20 A g^{-1}. Meanwhile, chemical vapor deposition can also be used in conjunction with other methods to
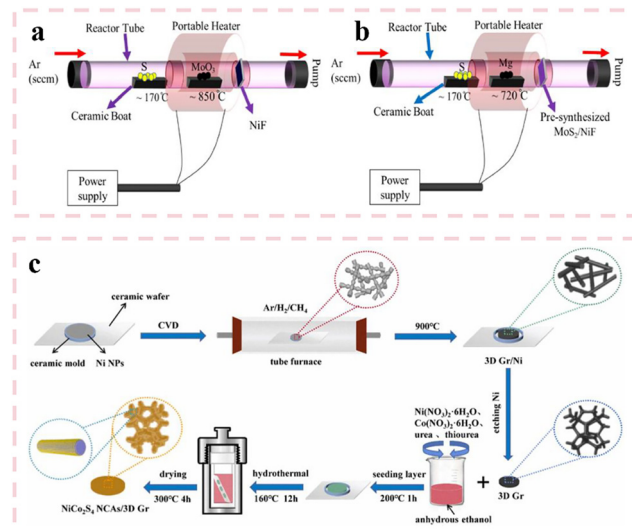

Fig. 5 Schematic diagram for the synthesis of (a) MoS_2 and (b) MgS/MoS_2@NiF EMs. Reproduced with permission from ref. 80. (c) Schematic of the preparation process of $NiCo_2S_4$ NCAs/3D Gr. Reproduced with permission from ref. 81.

construct more complex morphologies and structures. Therefore, materials synthesized by combining chemical vapor deposition with other methods generally show better performance than those synthesized by just chemical vapor deposition. As shown in Fig. 5(c), Zhang et al.[81] synthesized $NiCo_2S_4$ nanocone arrays (NCAs) using chemical vapor deposition and subsequent hydrothermal methods. First, 3D nanoparticles with small pore diameters were prepared by chemical vapor deposition. The small pores of 3D graphene (3D Gr) not only improved its conductivity, but also increased its contact area with the electrolyte solution. Then, $NiCo_2S_4$ NCAs were vertically grown on 3D Gr by a hydrothermal method. Due to the synergistic effect between 3D Gr and $NiCo_2S_4$ NCAs, the specific capacitance of $NiCo_2S_4$ NCAs/3D Gr electrode was 948.9 F g^{-1} at a current density of 1 A g^{-1}, and the capacitance retention at 10 A g^{-1} was 84.3% after 10 000 cycles. In addition, an ASC ($NiCo_2S_4$ NCAs/3D Gr/AC) also delivered a power density of 1153.8 W kg^{-1} and an energy density of 64.1 W h kg^{-1}. After 10 000 cycles, the capacitor can still maintain 90% of its initial specific capacitance. Besides, the CVD method can also be combined with the electrodeposition method. Yu et al.[82] synthesized a nano-honeycomb manganese cobalt sulfide/three-dimensional graphene foam nickel composite by a CVD method and electrodeposition method. Specifically, the three-dimensional graphene on foam nickel was prepared by the CVD method, and then depositing nano-honeycomb manganese cobalt sulfide on the as-prepared three-dimensional graphene by the electrodeposition method. The material showed a three-dimensional crossing porous structure. Due to this structure, the electrode exhibited a larger specific surface area in contact with the electrolyte, which can provide more active sites and enhanced electrochemical performance. The nano-honeycomb manganese cobalt sulfide/three-dimensional graphene foam nickel material delivered a specific capacitance of 1938 F g^{-1}

at a current density of 5 A g^{-1}. The specific capacitance of this material is 1320 F g^{-1} after 4000 cycles at a current density of 50 A g^{-1}. Notably, the material also showed excellent rate capability and maintained a specific capacitance retention of 76.8% at 100 A g^{-1}.

However, the reaction conditions of the chemical vapor deposition method are relatively harsh, especially, traditional CVD often requires extremely high temperatures. Although new technologies, e.g. laser-assisted technology, can reduce its reaction temperature, the chemical vapor deposition method has not been fully developed in the preparation of electrode materials for ASCs due to its excessively harsh reaction conditions.

In summary, various synthesis methods including hydrothermal synthesis, electrodeposition, and CVD methods, have been explored to synthesize advanced TMS-based electrodes. The hydrothermal method enables precise control over nanostructures (e.g., nanorods, porous structures) under mild reaction conditions, making it suitable for large-scale production. Electrodeposition allows uniform material deposition onto substrates with flexible process parameters (e.g., current density, deposition time). In contrast, CVD produces high-purity materials with dense structures, making it particularly effective for synthesizing delicate nanostructures such as nanosheet arrays. Despite these advantages, scaling up these synthesis methods for practical applications presents several key challenges. The hydrothermal method suffers from lengthy reaction times and difficulty maintaining uniformity during mass production. Electrodeposition is highly dependent on conductive substrates, leading to higher equipment costs. Additionally, CVD demands harsh reaction conditions (high temperature, vacuum), complex apparatus, and substantial energy consumption, increasing scalability costs.

4. Strategies for increasing specific capacitance

In recent years, researchers have conducted extensive research on nanostructured electrodes for high-performance supercapacitors. Especially, TMSs have attracted much attention due to their excellent conductivity, abundant redox active sites, and excellent electrochemical activity compared to transition metal oxides. However, their low specific capacitance and poor cycling stability—attributed to structural degradation during redox reactions—remain critical challenges. To address these limitations, researchers have developed methods to improve transition metal dichalcogenide performance. At present, we mainly optimize the structure of TMSs through elemental doping, introduction of sulfur vacancies, and conformity with carbon materials to improve the electrochemical performance of transition metal dichalcogenides.[83–86] In the following sections, we will highlight some of these details.

4.1. Element doping

Element doping is considered as one of the reliable strategies to improve capacitance performance and cycling stability by adjusting the morphology of electrode materials to increase electroactive sites and improve conductivity.[87] For example, Praphaiphon et al.[88] adjusted the morphology of NiCo$_2$S$_4$/Ni$_3$S$_2$ by doping Mn. Compared with pure electrodes, introduction of Mn could obtain thinner nanosheets and larger pores. Interestingly, it resulted in agglomeration on the electrode with the increasing of Mn amount. Both experiments and calculations indicated that doping Mn ions in the NiCo$_2$S$_4$ lattice could improve the interaction between electrolyte OH$^-$ ions and Co metal centers, thus enhancing the conductivity of the electrode. The experimental results showed that the maximum capacity of Mn doped electrodes is 145 mA h g^{-1} (1350 F g^{-1}), which is much higher than that of undoped electrodes. Meanwhile, it also maintained outstanding cycling stability and rate capability. Yan et al.[89] used a one-step hydrothermal method to prepare vanadium doped nickel sulfide (VNS) by using nickel foam as the nickel source. Due to the doping of vanadium, nickel sulfide was assembled into a nanoflower structure from nanosheets, which was conducive to charge exchange and electrolyte permeation during the reaction process. Benefiting from the unique structural features, the VNS electrode provided more active sites for redox reactions. Besides, the optimal ratio was also determined by controlling the doping amounts of V. When the V doping amount was 0.7 mmol, the specific capacitance of the electrode can reach 2072 F g^{-1} at a current density of 1 A g^{-1}. In addition, the HSC assembled with the VNS cathode and activated carbon anode also exhibited excellent performance. It delivered an energy density of 81.33 W h kg^{-1} at a power density of 160 W kg^{-1}. Notably, the HSCs can still maintain a capacitance retention rate of 82.2% after 10 000 charge and discharge cycles. As shown in Fig. 6(a), Lu et al.[90] fabricated a porous hollow structure integrating nitrogen-doped carbon quantum dots (NCDs) with NiCoS through a combined water bath and hydrothermal reaction strategy. This hierarchical hollow architecture synergistically enhances performance through three mechanisms: abundant active sites, internal electrolyte reservoirs, and optimized ion/electron transport pathways. The composite demonstrates a high specific capacity of 764.1 C g^{-1} at 1 A g^{-1}. The assembled supercapacitor based on the NCD/Ni$_{1.5}$Co$_1$S configuration exhibits remarkable energy density (73 mW h cm^{-2} at 1.39 W cm^{-2}) and exceptional cycling stability, retaining 96.5% of its initial capacity after 10 000 charge–discharge cycles. As shown in Fig. 6(b), Njemuwa Nwaji et al.[91] successfully synthesized iron-doped cubic cobalt-based MOFs, subsequently transforming them into sulfur vacancy-rich hollow core–shell nanocubes via a facile ambient-temperature conversion method. The iron doping effectively modulates the electronic structure, creating additional active sites and enabling efficient charge transfer, thereby significantly enhancing the electrochemical performance. At 10 A g^{-1}, the iron-doped material maintains 96.5% capacity retention after 6000 cycles, outperforming its undoped counterpart (84% retention). This improvement stems from the synergistic effects of sulfur vacancy engineering and optimized electron transport kinetics within the hollow heterostructure. As shown in Fig. 6(c), Cao et al.[92] prepared NiCo$_2$S$_4$@C and NiS@C composite nanoparticle samples by using solvothermal and chemical vapor
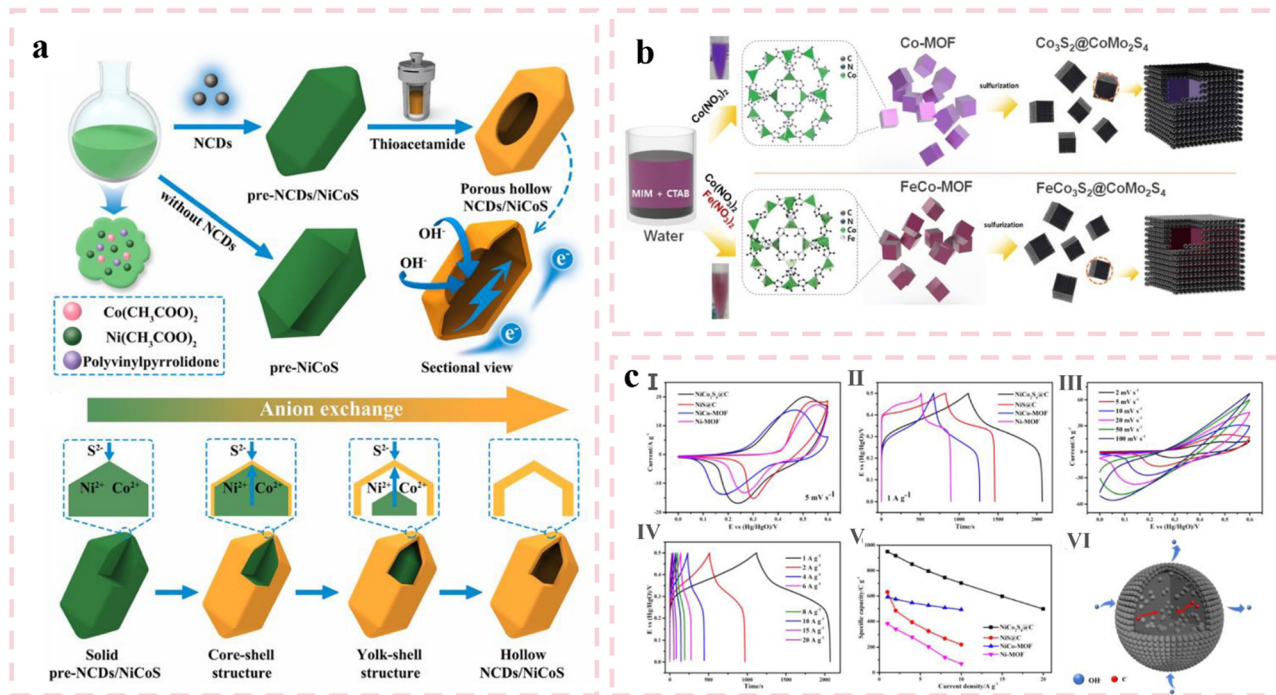
Fig. 6 (a) Schematic illustration of the preparation of NCDs/NiCoS nanocomposites and the formation of the hollow structure. Reproduced with permission from ref. 90. (b) Schematic illustration of the two-step synthetic route for vacancy engineered nanostructures. Reproduced with permission from ref. 91. (c) (I) CV and (II) GCD curves of NiCo$_2$S$_4$@C, NiS@C, NiCo-MOF and Ni-MOF electrodes, (III) CV curves of the NiCo$_2$S$_4$@C electrode, and (IV) GCD curves of the NiCo$_2$S$_4$@C electrode. (V) Specific capacity of NiCo$_2$S$_4$@C, NiS@C, NiCo-MOF and Ni-MOF electrodes measured at different current densities. (VI) Schematic illustration of the sulfide microsphere composed of carbon-coated nanoparticles. Reproduced with permission from ref. 91.

deposition methods. The SEM and TEM images further revealed the introduction of Co in the bimetallic MOF could increase the porosity of the material, resulting in a rougher surface of the sphere. The increase in porosity was more conducive to the penetration of electrolyte into electrode materials, and provided more active sites to increase capacity. Notably, for a current density from 1 to 10 A g^{-1}, the specific capacitance retention of bimetallic nickel-based electrodes NiCo$_2$S$_4$@C was 73.9% and 83.2% for NiCo MOF, and the specific capacity retention of single metal nickel-based electrodes NiS@C was 34.9%, and for Ni MOF was 18%. Thanks to the structural characteristics of nanoparticles and the advantages of multi-component composite materials, the specific capacity of bimetallic NiCo-MOF is 948.9 C g^{-1} at a current density of 1 A g^{-1}. In contrast, the single-metal Ni MOF exhibited a lower specific capacity of 631.0 C g^{-1} from NiCo$_2$S$_4$@C. The ASC provided an excellent energy density of 43.8 W h kg^{-1} at a power density of 799.1 kW kg^{-1} at a voltage of 1.6 V.

Meanwhile, emerging ternary TMSs have demonstrated superior electrical conductivity and redox activity. Lai et al.[93] successfully synthesized Fe-doped NiCo$_2$S$_4$ nanosheets on N,S-doped ordered mesoporous carbon (N,S-CMK-3), creating an Fe–NiCo$_2$S$_4$@N,S-CMK-3 composite. Fe doping endows Fe–NiCo$_2$S$_4$ with enhanced electronic conductivity and higher adsorption enthalpy toward ionic liquid electrolytes, which collectively contribute to the excellent electrochemical performance. Notably, an ASC device assembled with a Fe–NiCo$_2$S$_4$ cathode electrode and N,S-CMK-3 anode electrode achieved a

high energy density of 107.5 W h kg^{-1} at a power density of 100 W kg^{-1}, accompanied by a wide operating voltage window of 4 V.

4.2. Introduction of sulfur vacancies

The presence of sulfur vacancies can reduce band gaps and increase carrier density, thereby significantly enhancing electronic conductivity and facilitating faster electron and ion transport.[94] The main method to create sulfur vacancies in TMS include argon plasma low-pressure treatment, pulsed laser deposition (PLD), and reduction. Among them, the reduction method is a facile way to introduce vacancies in sulfides by using reducing agents, such as glucose,[95] hydrazine,[96] and NaBH$_4$.[97] NaBH$_4$ is a mild reducing agent with many advantages such as simplicity, low energy consumption, safety, and room temperature reaction.[98] The presence of sulfur vacancies can optimize electronic structures, effectively improve interfacial reaction activity, and promote reaction kinetics. Meanwhile, these vacancies are also considered as electrochemical active sites, and further enhance capacity.[96,99] Therefore, supercapacitors assembled from electrode materials with sulfur vacancies exhibit favorable electrochemical performance. Zong et al.[100] synthesized sulfur vacancy-rich Bi$_2$S$_3$ anchored on nitrogen-doped carbon nanofibers (S-NCNF) via a simple solvothermal method, followed by high-temperature annealing. The resulting dr-Bi$_2$S$_3$/S-NCNF composite features a supporting matrix of nitrogen-doped carbon nanofibers uniformly coated with bismuth sulfide nanoparticles enriched in sulfur vacancies.

Due to the incorporation of sulfur vacancies, the material exhibits excellent electrochemical performance. DFT calculations further revealed that the adsorption energy of OH^- ions on dr-Bi_2S_3/S-NCNF (-3.15 eV) is much lower than that on df-Bi_2S_3/S-NCNF (-3.06 eV), indicating that the initial adsorption of OH^- ions more readily occurred on the surface of the dr-Bi_2S_3/S-NCNF electrode, thereby accelerating the subsequent faradaic reactions. Notably, an ASC assembled with dr-Bi_2S_3/S-NCNF and S-NCNF achieved a high energy density of 22.2 W h kg^{-1} at a power density of 677.3 W kg^{-1}. Li et al.[101] prepared sulfur vacancy enhanced cobalt molybdenum sulfide nanosheet (Vs CMS) integrated cathodes by using hydrothermal and $NaBH_4$ reduction methods. Due to the introduction of sulfur vacancies, the surface morphology of CMS nanosheets was greatly changed. The introduced nanosheets were interconnected to form a honeycomb-like microstructure, resulting in a rough surface and a larger specific surface area of the electrode material. Introducing sulfur vacancies in CMS not only provided more active sites for the two-phase redox reaction, but also accelerated the electron transfer. This synergistic effect arises from the combination of increased active sites provided by sulfur vacancies and improved charge transport facilitated by the layered structure, the optimal Vs-CMS integrated cathode displayed a high area capacity of 0.56 mA h cm^{-2} at 1 mA cm^{-2}, good rate performance of 0.34 mA h cm^{-2} at 30 mA cm^{-2}, and cycling stability of 96.7% after 10 000 cycles. In addition, the capacitive porous framework activated carbon (PFAC) anode was coupled with the optimal Vs CMS cathode for assembling HSC. The obtained PFAC anode delivered a high specific capacitance of 112.1 F g^{-1} at 0.25 A g^{-1}, a high-rate capacity of 46.3 F g^{-1} at 10 A g^{-1}, and good cycling stability of 95.5% after 10 000 cycles. The maximum energy density of the assembled HSC was 73.2 W h kg^{-1}, and the power density was 3014.7 W kg^{-1}. Besides, it exhibited excellent cycling stability of 93.3% after 10 000 cycles. Qu et al.[102] prepared rich sulfur-vacancy NiS (r-Ni_3S_2) by hydrothermal and $NaBH_4$ reduction processes. The r-Ni_3S_2 electrode material was in a shape of pleated nanoparticles, which were composed of petal-like flakes. Due to the larger specific surface area and sulfur vacancies, more active sites are exposed, so that the Gibbs free energy was reduced, resulting in a significant improvement in electrochemical performance. Impressively, the specific capacitance is 1571.8 F g^{-1} at a current density of 1 A g^{-1}, and the capacitance retention rate is 32%, higher than that of the original nickel sulfide. In addition, the ASC composed of r-Ni_3S_2 also showed excellent performance with an energy density of 33.7 W h kg^{-1} at a power density of 1167.8 W kg^{-1}. In addition to the $NaBH_4$ reduction method, other methods can be used to introduce sulfur vacancies. Qian et al.[103] synthesized hollow zinc–cobalt sulfide dodecahedron with abundant sulfur vacancies ($Zn_xCo_{3-x}S_4$) by co-precipitation and solvothermal vulcanization. The abundant sulfur vacancies and hollow dodecahedral structure delivered a large specific surface area, high electronic conductivity and mass transfer efficiency of the $Zn_xCo_{3-x}S_4$ electrode, which is conducive to improving the electrochemical performance of supercapacitors. Notably, the prepared $Zn_{0.3}Co_{2.7}S_4$ electrode displayed an enhanced specific capacitance of 545.9 C g^{-1} at a current density of 1 A g^{-1} along with a high capacitance retention rate of 84.7%

after 1000 cycles. In addition, the supercapacitor assembled by $Zn_{0.3}Co_{2.7}S_4$ and activated carbon also delivered excellent performance with a high energy density of 15.58 W h kg^{-1} at a power density of 800.11 W kg^{-1} as well as a capacity retention rate of 71.2% after 5000 cycles at a current density of 4 A g^{-1}. Huang et al.[104] synthesized hollow carbon-coated nickel sulfide nanocrystals (H–NiS_{1-x}/C) with sulfur vacancies by an ion exchange strategy and subsequent thermal annealing. Thanks to its hollow structure and sulfur vacancy, the optimal S-vacancy sample (H–NiS_{1-x}/C-50) exhibited a high specific capacitance of 1728 F g^{-1} at a current density of 1 A g^{-1}. After 8000 cycles, it could still maintain 72% of the initial specific capacitance. The ASC assembled by H–NiS_{1-x}/C-50 also achieved a high energy density of 36.88 W h kg^{-1}. As shown in Fig. 7(a), Cui et al.[105] developed a PS–NiS/Co_9S_8@NC composite featuring molecular-level NiS/Co_9S_8 heterojunctions, sulfur vacancies (SVs), and nitrogen-doped carbon (NC) coatings. The atomic-scale heterojunction engineering, combined with the polyhedral star-like nanostructure, synergistically increased active site exposure and optimized interfacial electron environments. The SV defects and NC coating collectively enhanced electrical conductivity and charge transfer kinetics. This structural optimization resulted in an outstanding specific capacitance of 1902 F g^{-1} at 1 A g^{-1}, along with reliable cycling stability—80.1% capacitance retention after 7000 cycles. The hierarchical design effectively balances high energy storage capacity with long-term durability. As shown in Fig. 7(b), Shao et al.[106] enhanced the electrochemical performance of Fe_7S_8 through dual modification with phosphorus doping and sulfur vacancies. The P–Fe_7S_8 electrode demonstrated exceptional cycling stability, retaining 84.9% of its initial specific capacity after 8000 cycles—significantly superior to Fe_3S_4 counterparts. Furthermore, the assembled NiS//P–Fe_7S_8 asymmetric supercapacitor achieved a high energy density of 134.8 W h kg^{-1} at a power density of 1042.1 W kg^{-1}, showcasing remarkable energy-power balance. As shown in Fig. 7(c), Tian et al.[107] synthesized a 3D sea-urchin-like $NiCo_2S_4$/C composite via a one-step sulfidation-carbonization strategy using NiCo-based metal–organic frameworks (MOFs) as templates. Precise control of the Co/Ni ratio optimized interfacial interactions, generating structural defects and synergistic effects between the two metals to enhance electrochemical activity. During high-temperature pyrolysis, the nanorods underwent contraction and structural remodeling, forming fibrous carbon matrices. The in situ formed $NiCo_2S_4$ nanoparticles were uniformly dispersed within the carbon framework, creating abundant active sites and efficient charge transport pathways. The composite exhibited a high specific capacitance of 1934 F g^{-1} at 1 A g^{-1} with excellent rate capability. The assembled hybrid supercapacitor delivered an energy density of 50.24 W h kg^{-1} at 800 W kg^{-1}, demonstrating practical energy storage potential (Table 1).

4.3. Composite with carbon materials

It is well established that the charge storage capability of TMS is significantly influenced by their structural and morphological features, such as surface area, porosity, and crystallinity. Thus, the rational design and synthesis of nanostructured materials
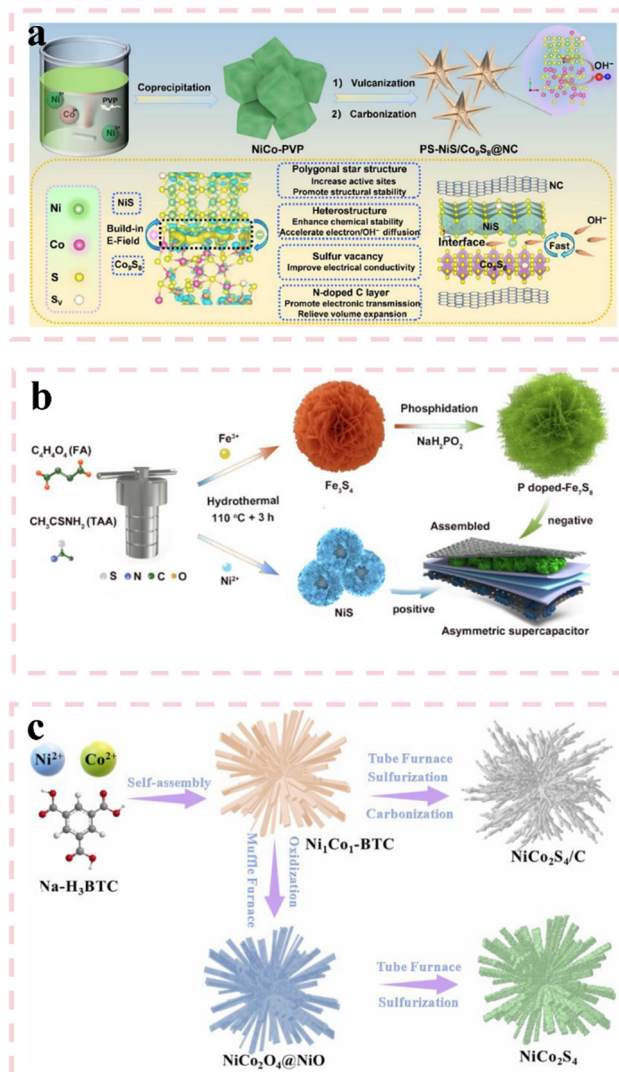
Fig. 7 (a) Synthesis procedure and structure function of the polyhedral star PS−NiS/Co$_9$S$_8$@NC. Reproduced with permission from ref. 105. (b) Schematic illustration for the formation of P−Fe$_7$S$_8$ and NiS as electrode materials for the ASC. Reproduced with permission from ref. 106. (c) Schematic illustration of the fabrication routes of Ni$_1$Co$_1$−BTC, NiCo$_2$O$_4$@-NiO (NCO), NiCo$_2$S$_4$/C (NCSC) and NiCo$_2$S$_4$ (NCS). Reproduced with permission from ref. 107.

are pivotal for optimizing the electrochemical performance of TMS-based electrodes, primarily due to enhanced active site exposure and improved ion diffusion pathways. Carbon-based materials, particularly those with high specific surface areas,

excellent electrical conductivities, and hierarchical porous structures, are ideal candidates for hybridization with TMS. These properties facilitate efficient charge transport and provide abundant redox-active sites. At present, hollow/porous transition metal sulfide/carbon composites have attracted extensive attention due to their abundant redox active sites, excellent structural roughness, large surface area and shortened ion diffusion path.[110,111] As shown in Fig. 8(a), Fan et al.[109] synthesized NiCo$_2$S$_4$-reduced graphene oxide (NiCo$_2$S$_4$-rGO) composites by a hydrothermal method. The TEM image showed that NiCo$_2$S$_4$-rGO (16%) displayed a hierarchical porous structure composed of rGO nanosheets, and this integrated structure could greatly improve the electron transport and specific surface area, and provide sufficient active sites for redox reactions. Thanks to the synergistic effect between NiCo$_2$S$_4$ and rGO, the NiCo$_2$S$_4$-rGO composite maintained 90% of its initial specific capacitance after 5000 cycles at 5 A g^{-1}, while the NiCo$_2$S$_4$ only maintained 48% of the initial specific capacitance under the same conditions. In addition, the assembled ASC in which the NiCo$_2$S$_4$-rGO composite served as the positive electrode and porous carbon skeleton-rGO was employed as the negative electrode, also showed excellent electrochemical properties. Notably, the device delivered a high energy density of 35 W h kg^{-1} and excellent cycling performance with a capacitance retention rate of 95% after 8000 cycles. In addition to coupling with reduced graphene oxide, NiCo$_2$S$_4$ can also be combined with other carbon materials. Li et al.[112] synthesized NiCo$_2$S$_4$ nanoparticle composites on the inner surface of lignin-derived 3D hierarchical porous carbon (HPC) in situ by a one-step solvothermal method. The SEM results showed that the NiCo$_2$S$_4$ nanoparticles spontaneously stacked and connected with each other before recombination with HPC, which greatly limited the exposure of active sites on the surface. However, after the recombination of NiCo$_2$S$_4$ nanoparticles and HPC, NiCo$_2$S$_4$ nanoparticles were grown on the surface of the HPC. This composite structure effectively avoided the aggregation of nanoparticles and increased the specific surface area of NiCo$_2$S$_4$ composites, so that more active sites were exposed to the electrolyte and improved the electrochemical performance. The NiCo$_2$S$_4$/HPC composites exhibited an excellent specific capacitance of 1264.2 F g^{-1} at a current density of 1 A g^{-1}. At the same time, the ASC assembled with the NiCo$_2$S$_4$/HPC positive electrode and activated carbon negative electrode also obtained excellent electrochemical properties with an energy density of 32.05 W h kg^{-1} at a power density of 193.9 W kg^{-1}. As shown in Fig. 8(b), Zhang et al.[108]

Table 1 Performance comparison of TMS synthesized by different enhancement strategies

Material	Specific capacitance (F g^{-1})	Cycling performance	Enhancement strategies	Ref.
V-Ni$_3$S$_2$	2072 (1 A g^{-1})	82.2% (10 000 cycles)	Element doping	89
NCDs/Ni$_2$CoS	1698 (1 A g^{-1})	96.5% (10 000 cycles)	Element doping	90
r-Ni$_3$S$_2$	1571 (1 A g^{-1})	74% (5000 cycles)	Sulfur vacancies	102
NiCo$_2$S$_4$/C	1934 (1 A g^{-1})	93.2% (5000 cycles)	Sulfur vacancies	107
NiS/rGO	2157 (2 A g^{-1})	92.4% (30 000 cycles)	Composite with carbon materials	108
NiCo$_2$S$_4$-rGO	1260 (1 A g^{-1})	90% (5000 cycles)	Composite with carbon materials	109
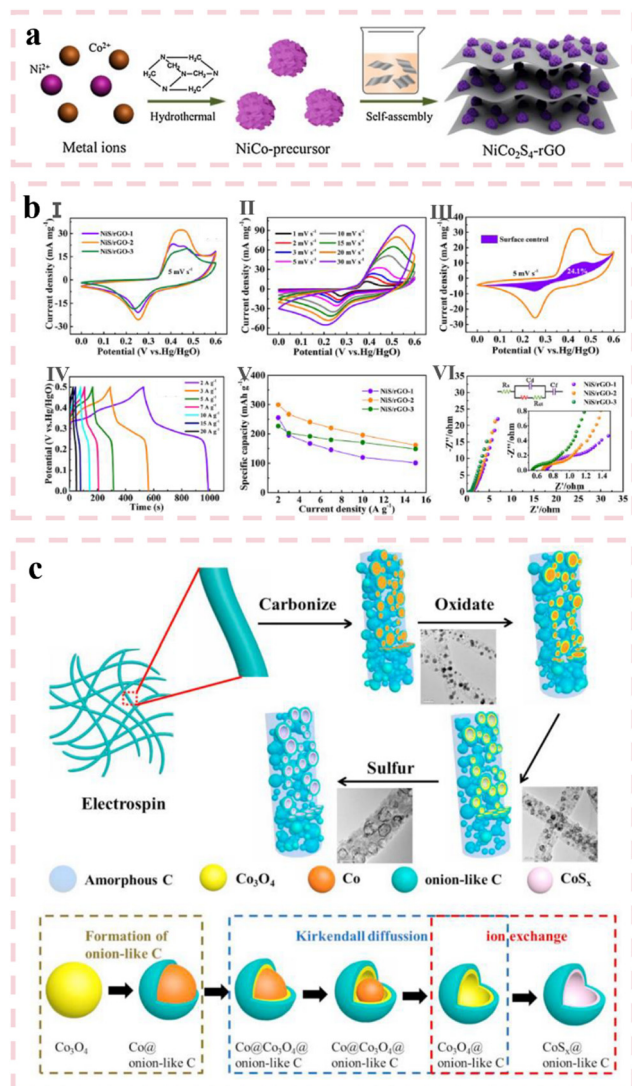
Fig. 8 (a) Schematic illustration of the fabrication procedure for NiCo$_2$S$_4$-rGO composites. Reproduced with permission from ref. 109. (b) (I) CV curves of the prepared NiS/rGO nanocomposites, (II) CV curves of the NiS/rGO-2 sample at different scan rates and (III) the NiS/rGO-2 sample, (IV) GCD curves of the NiS/rGO-2 sample under different current densities, (V) rate performance of the prepared NiS/rGO nanocomposites, and (VI) Nyquist plots of the NiS/rGO-2 sample. Reproduced with permission from ref. 108. (c) Schematic illustration of the designed electrode fabrication process and the formation mechanism of CoSx HNPs covered with onion-like carbon. Reproduced with permission from ref. 113.

prepared NiS/reduced graphene oxide nanocomposites by high-temperature calcination. Compared with the initial NiS, the dispersion, size and morphology of NiS nanoparticles loaded on the surface of reduced graphene oxide were significantly improved. The limited space between the graphene oxide layers restricted the agglomeration of Ni nanoparticles, ensuring the uniform dispersion of Ni nanoparticles. When Ni nanoparticles were converted to NiS by vulcanization reaction with elemental sulfur, the well-dispersed NiS nanoparticles formed a loose layered structure and were loaded on well-separated GO nanosheets, thereby obtaining excellent electrochemical properties. The

NiS/rGO nanocomposites delivered an ultra-high specific capacitance of 299.7 mA h g^{-1} at a current density of 2 A g^{-1}. At the same time, the composite material also presented a favorable rate capability, and a specific capacitance of 161.2 mA h g^{-1} at a current density of 15 A g^{-1}. In addition, the composite-based supercapacitors also exhibited excellent electrochemical performance, providing an energy density of 56.1 W h kg^{-1} at a specific power density of 880 W kg^{-1}. Meanwhile, the device also showed excellent cycling stability with a high capacitance retention rate of 92.4% after 30 000 cycles. As shown in Fig. 8(c), Liu et al.[113] synthesized a CoS$_x$/C hybrid nanofiber architecture through a combined electrospinning and hydrothermal strategy. The CoS$_x$/C nanofibers feature CoS$_x$ hollow nanoparticles (HNPs) encapsulated within porous carbon nanofibers (PCNFs), endowing the material with multiple structural merits. Firstly, the PCNF matrix effectively confines the migration of Co^{2+} and S^{2-} ions, preventing their aggregation while providing buffer space to accommodate volume expansion of TMS during cycling. Additionally, the onion-like carbon layers enveloping the CoS$_x$ HNPs significantly enhance the overall electrical conductivity of the hybrid electrode, thereby optimizing its electrochemical kinetics. The asymmetric supercapacitor assembled with CoS$_x$/C hybrid//PCNF electrodes demonstrates a high energy density of 15.0 W h kg^{-1} at a power density of 413 kW kg^{-1}, showcasing its potential for high-power energy storage applications.

5. Conclusions

In this paper, important advances of TMS and its composites in supercapacitors have been summarized, and various strategies to enhance the electrochemical performance of TMS have been highlighted and critically evaluated. Due to their excellent electrical conductivity, high specific capacitance, low production cost, and versatile structural configurations, TMS materials exhibit significant potential for use in ASCs, and there are still some challenges and issues that need to be addressed for further commercial application of ASCs.

(1) The electrochemical performance of transition metal sulfides (TMS) is closely intertwined with their nanostructures. Therefore, researchers should pay more attention to the morphological regulation of TMS. By integrating atomic-level regulation with nanoengineering, it becomes possible to address the trade-offs among energy density, cycle life, and scalable production. Besides, it is necessary to shift from "performance-oriented" laboratory research to "cost-performance balanced" industrial development. Meanwhile, incorporating computational materials science and green processing techniques will be crucial to bridging the gap between academic innovation and real-world implementation.

(2) While most TMS studies are based on experimental observations, there remain significant challenges in scaling up these materials for industrial production and practical operation. Bridging the gap between lab-scale experiments and large-scale manufacturing is crucial for realizing the full potential of TMS. To better understand the intricate

relationship between nanostructures and electrochemical properties of TMS, greater emphasis should be placed on developing robust mathematical models and conducting detailed simulation calculations. These efforts will guide researchers in designing more rational structures with enhanced performance. Although this work is extremely challenging, it will provide valuable guidance for researchers to construct more rational structure.

(3) One of the primary limitations of ASCs remains their insufficient energy density. Beyond optimizing cathode materials, careful selection of suitable anode materials and electrolytes is essential. Research into developing advanced anode materials and electrolytes with superior performance is critical for enhancing overall device performance and advancing commercialization. However, there is still a lack of relevant research, and the development of anode materials and electrolytes with excellent performance is of great significance in the commercialization process of ASCs.

(4) The synthesis method is usually complicated and expensive. In order to meet the needs of commercial application and large-scale production, it is still necessary to explore a low-cost and simple synthesis method to prepare high-performance electrode materials.

(5) Current research places excessive emphasis on single performance indicators such as specific capacitance and energy density, but lacks a systematic evaluation of the feasibility of large-scale production (such as the scaling-up effect of the synthesis process and equipment compatibility), resulting in most of the achievements remaining at the theoretical level and being difficult to translate into practical applications. In the future, production feasibility indicators (such as synthesis yield, equipment compatibility, and cost models) can be introduced at the material design stage to make "manufacturability" a core parameter in research and design.

Data availability

No primary research results, software or code have been included and no new data were generated or analysed as part of this review.

Conflicts of interest

There are no conflicts to declare.

Acknowledgements

Notes and references

1 X. Yang, Y. Song, G. Wang and W. Wang, *IEEE Trans. Sustain. Energy*, 2010, **1**, 57–65.
2 G. Wang, L. Zhang and J. J. C. S. R. Zhang, *Chem. Soc. Rev.*, 2012, **41**, 797–828.
3 Y. Pan, C. Shi, Y. Chen, D. Li, Z. Tian, L. Guo and Y. Wang, *Appl. Surf. Sci.*, 2021, **566**, 150744.
4 R. Rajak, R. Kumar, S. N. Ansari, M. Saraf and S. M. Mobin, *Dalton Trans.*, 2020, **49**, 11792–11818.
5 B. Chang, W. Shi, S. Han, Y. Zhou, Y. Liu, S. Zhang and B. Yang, *Chem. Eng. J.*, 2018, **350**, 585–598.
6 T. Xu, G. Li, X. Yang, Z. Guo and L. Zhao, *Chem. Eng. J.*, 2019, **362**, 783–793.
7 Z. Wang, J. Cheng, J. Zhou, J. Zhang, H. Huang, J. Yang, Y. Li and B. Wang, *Nano Energy*, 2018, **50**, 106–117.
8 L. L. Zhang and X. Zhao, *Chem. Soc. Rev.*, 2009, **38**, 2520–2531.
9 A. Borenstein, O. Hanna, R. Attias, S. Luski, T. Brousse and D. Aurbach, *J. Mater. Chem. A*, 2017, **5**, 12653–12672.
10 A. González, E. Goikolea, J. A. Barrena and R. Mysyk, *Renewable Sustainable Energy Rev.*, 2016, **58**, 1189–1206.
11 W. Raza, F. Ali, N. Raza, Y. Luo, K.-H. Kim, J. Yang, S. Kumar, A. Mehmood and E. E. Kwon, *Nano Energy*, 2018, **52**, 441–473.
12 E. Bao, X. Ren, R. Wu, X. Liu, H. Chen, Y. Li and C. Xu, *J. Colloid Interface Sci.*, 2022, **625**, 925–935.
13 M. Z. Iqbal, M. M. Faisal, S. R. Ali and M. Alzaid, *Solid State Ionics*, 2020, **354**, 115411.
14 J. Yan, Q. Wang, T. Wei and Z. Fan, *Adv. Energy Mater.*, 2014, **4**, 1300816.
15 Y. Wang and Y. Xia, *Adv. Mater.*, 2013, **25**, 5336–5342.
16 R. Wu, J. Sun, C. Xu and H. Chen, *Sustainable Energy Fuels*, 2021, **5**, 4807–4829.
17 R. Khezri, S. R. Motlagh, M. Etesami, A. A. Mohamad, F. Mahlendorf, A. Somwangthanaroj and S. Kheawhom, *Chem. Eng. J.*, 2022, **449**, 137796.
18 A. M. Zardkhoshoui and S. S. H. Davarani, *Sustainable Energy Fuels*, 2021, **5**, 900–913.
19 A. M. Zardkhoshoui, S. S. H. Davarani, M. M. Ashtiani and M. Sarparast, *J. Mater. Chem. A*, 2019, **7**, 10282–10292.
20 M. Zhi, C. Xiang, J. Li, M. Li and N. Wu, *Nanoscale*, 2013, **5**, 72–88.
21 S. E. Moosavifard, F. Saleki, A. Mohammadi, A. Hafizi and M. R. Rahimpour, *J. Electroanal. Chem.*, 2020, **871**, 114295.
22 J. Ge, J. Meng, L. Zhang, J. Qin, G. Yang, Y. Wu, H. Zhu, Y. Huang, E. Debroye and H. Dong, *Small*, 2024, **20**, 2312019.
23 J. Hu, L. Sun, F. Xie, Y. Qu, H. Tan and Y. Zhang, *J. Mater. Chem. A*, 2023, **11**, 8380–8391.
24 C. Ni, X. Wang, X. Cai, C. Yu, Q. Wu, Y. Shen and C. Hao, *J. Mater. Sci. Technol.*, 2025, **210**, 233–245.
25 L. Shen, L. Yu, H. B. Wu, X.-Y. Yu, X. Zhang and X. W. Lou, *Nat. Commun.*, 2015, **6**, 6694.
26 W. He, C. Wang, H. Li, X. Deng, X. Xu and T. Zhai, *Adv. Energy Mater.*, 2017, **7**, 1700983.
27 Y. Zhao, Z. Shi, H. Li and C.-A. Wang, *J. Mater. Chem. A*, 2018, **6**, 12782–12793.
28 W. Zong, C. Yang, L. Mo, Y. Ouyang, H. Guo, L. Ge, Y.-E. Miao, D. Rao, J. Zhang and F. Lai, *Nano Energy*, 2020, **77**, 105189.
29 C. Yang, J. Feng, Y. Zhang, Q. Yang, P. Li, T. Arlt, F. Lai, J. Wang, C. Yin and W. Wang, *Small*, 2019, **15**, 1903720.
30 C. Dong, L. Guo, H. Li, B. Zhang, X. Gao, F. Tian, Y. Qian, D. Wang and L. Xu, *Energy Storage Mater.*, 2020, **25**, 679–686.
31 M. Ma, Y. Yao, Y. Wu and Y. Yu, *Adv. Fiber Mater.*, 2020, **2** 314–337.
32 C. Wang, C. Zhao, X. Pu, Y. Zeng, Y. Wei, Y. Cao and Z. Chen, *ACS Appl. Mater. Interfaces*, 2024, **16**, 17637–17648.
33 C. Qu, Y. Jiao, B. Zhao, D. Chen, R. Zou, K. S. Walton and M. Liu, *Nano Energy*, 2016, **26**, 66–73.
34 C. Young, J. Kim, Y. V. Kaneti and Y. Yamauchi, *ACS Appl. Energy Mater.*, 2018, **1**, 2007–2015.
35 C. Chen, M.-K. Wu, K. Tao, J.-J. Zhou, Y.-L. Li, X. Han and L. Han, *Dalton Trans.*, 2018, **47**, 5639–5645.
36 J. Chmiola, G. Yushin, Y. Gogotsi, C. Portet, P. Simon and P.-L. Taberna, *Science*, 2006, **313**, 1760–1763.
37 Y. Zhai, Y. Dou, D. Zhao, P. F. Fulvio, R. T. Mayes and S. Dai, *Adv. Mater.*, 2011, **23**, 4828–4850.

38 X. Zhao, B. M. Sánchez, P. J. Dobson and P. S. Grant, *Nanoscale*, 2011, **3**, 839–855.

39 J. T. Mefford, W. G. Hardin, S. Dai, K. P. Johnston and K. J. Stevenson, *Nat. Mater.*, 2014, **13**, 726–732.

40 P. Simon and Y. Gogotsi, *Acc. Chem. Res.*, 2013, **46**, 1094–1103.

41 J.-S. M. Lee, M. E. Briggs, C.-C. Hu and A. I. Cooper, *Nano Energy*, 2018, **46**, 277–289.

42 S. Zhang, Y. Liu, Q. Han, S. He, N. Zhang and J. Yang, *J. Alloys Compd.*, 2017, **729**, 850–857.

43 M. M. Baig, I. H. Gul, S. M. Baig and F. Shahzad, *J. Energy Storage*, 2021, **44**, 103370.

44 B. Xu, F. Wu, S. Chen, C. Zhang, G. Cao and Y. Yang, *Electrochim. Acta*, 2007, **52**, 4595–4598.

45 A. Balducci, U. Bardi, S. Caporali, M. Mastragostino and F. Soavi, *Electrochem. Commun.*, 2004, **6**, 566–570.

46 Y. Fang, J. Liu, D. J. Yu, J. P. Wicksted, K. Kalkan, C. O. Topal, B. N. Flanders, J. Wu and J. Li, *J. Power Sources*, 2010, **195**, 674–679.

47 Y. Qin, J. Yuan, J. Li, D. Chen, Y. Kong, F. Chu, Y. Tao and M. Liu, *Adv. Mater.*, 2015, **27**, 5171–5175.

48 Y. Qin, J. Yuan, L. Zhang, B. Zhao, Y. Liu, Y. Kong, J. Cao, F. Chu, Y. Tao and M. Liu, *Small*, 2016, **12**, 2549–2553.

49 V. V. Obreja, *Phys. E*, 2008, **40**, 2596–2605.

50 R. Dubey and V. Guruviah, *Ionics*, 2019, **25**, 1419–1445.

51 A. Ehsani, M. Bigdeloo, F. Assefi, M. Kiamehr and R. Alizadeh, *Inorg. Chem. Commun.*, 2020, **115**, 107885.

52 F. Béguin, K. Kierzek, M. Friebe, A. Jankowska, J. Machnikowski, K. Jurewicz and E. Frackowiak, *Electrochim. Acta*, 2006, **51**, 2161–2167.

53 S. W. Lee, J. Kim, S. Chen, P. T. Hammond and Y. Shao-Horn, *ACS Nano*, 2010, **4**, 3889–3896.

54 D. Zhang, H. Yan, Y. Lu, K. Qiu, C. Wang, C. Tang, Y. Zhang, C. Cheng and Y. Luo, *Nanoscale Res. Lett.*, 2014, **9**, 1–9.

55 A. Muzaffar, M. B. Ahamed, K. Deshmukh and J. Thirumalai, *Renewable Sustainable Energy Rev.*, 2019, **101**, 123–145.

56 H. D. Mai, K. Rafiq and H. Yoo, *Chem. – Eur. J.*, 2017, **23**, 5631–5651.

57 F. Zhang, T. Zhang, X. Yang, L. Zhang, K. Leng, Y. Huang and Y. Chen, *Energy Environ. Sci.*, 2013, **6**, 1623–1632.

58 J. Xie, X. Sun, N. Zhang, K. Xu, M. Zhou and Y. Xie, *Nano Energy*, 2013, **2**, 65–74.

59 S. Dai, B. Zhao, C. Qu, D. Chen, D. Dang, B. Song, B. M. Deglee, J. Fu, C. Hu and C.-P. Wong, *Nano Energy*, 2017, **33**, 522–531.

60 Q. Li, W. Lu, Z. Li, J. Ning, Y. Zhong and Y. Hu, *Chem. Eng. J.*, 2020, **380**, 122544.

61 Y. Sun, Y. Wang, C. Wang, J. Wang, Z. Wang, M. Zhang, H. Zong, J. Xu and J. Liu, *Chem. Eng. J.*, 2023, **469**, 143812.

62 A. Asghar, M. I. Yousaf, N. A. Shad, M. Munir Sajid, A. M. Afzal, Y. Javed, A. Razzaq, M. Shariq, Q.-U.-A. Gulfam and M. Sarwar, *J. Cluster Sci.*, 2022, **33**, 2325–2335.

63 G. Jiang, R. A. Senthil, Y. Sun, T. R. Kumar and J. Pan, *J. Power Sources*, 2022, **520**, 230886.

64 R. A. Senthil, S. Osman, J. Pan, X. Liu and Y. Wu, *J. Energy Storage*, 2021, **44**, 103263.

65 J. Balamurugan, C. Li, T. D. Thanh, O.-K. Park, N. H. Kim and J. H. Lee, *J. Mater. Chem. A*, 2017, **5**, 19760–19772.

66 Y. Yan, S. Ding, X. Zhou, O. Hu, Y. Feng, Q. Zheng, D. Lin and X. Wei, *J. Alloys Compd.*, 2021, **867**, 158941.

67 H. Gonenc and B. Scholtens, *Ecol. Econ.*, 2017, **132**, 307–328.

68 S. Wang, P. Zhang and C. Liu, *Colloids Surf., A*, 2021, **616**, 126334.

69 J. Gou, S. Xie and B. Xu, *Ionics*, 2020, **26**, 337–344.

70 J. Gou, S. Xie, Z. Yang, Y. Liu, Y. Chen, Y. Liu and C. Liu, *Electrochim. Acta*, 2017, **229**, 299–305.

71 K. Moorthi, J. Yesuraj, K. Kim, M. Padaki and S. Mohan, *J. Energy Storage*, 2024, **100**, 113474.

72 M. M. Faisal, S. R. Ali, S. S. Shah, M. W. Iqbal, S. Pushpan, M. A. Aziz, N. P. Aguilar, M. M. A. Rodríguez, S. L. Loredo and K. Sanal, *Ceram. Int.*, 2022, **48**, 28565–28577.

73 C. Ni, R. Chen, C. Hao, Y. Lu, J. Wu, Y. Shen and X. Wang, *J. Alloys Compd.*, 2023, **960**, 170807.

74 X. Yang, J. Mao, H. Niu, Q. Wang, K. Zhu, K. Ye, G. Wang, D. Cao and J. Yan, *Chem. Eng. J.*, 2021, **406**, 126713.

75 Y.-F. Wang, S.-X. Zhao, L. Yu, X.-X. Zheng, Q.-L. Wu and G.-Z. Cao, *J. Mater. Chem. A*, 2019, **7**, 7406–7414.

76 F. Ma, X. Dai, J. Jin, N. Tie and Y. Dai, *Electrochim. Acta*, 2020, **331**, 135459.

77 X. Pu, X. Ren, H. Yin, Y. Tang and H. Yuan, *J. Alloys Compd.*, 2021, **865**, 158736.

78 A. George and M. Kundu, *Energy Fuels*, 2023, **37**, 12369–12380.

79 L. Zhao, S. Lei, C. Tang, Q. Tu, L. Rao, H. Liao, W. Zeng, Y. Xiao and B. Cheng, *J. Colloid Interface Sci.*, 2022, **616**, 401–412.

80 A. Raza, A. Farid, M. Yousaf, A. M. Alfares, A. Rasheed, I. Khan, M. A. Ghanem and K. M. Mohammed, *Electrochim. Acta*, 2024, **497**, 144579.

81 H. Zhang, Y. Xie, S. Yang, X. Gao, H. Bai, F. Yao and H. Yue, *J. Alloys Compd.*, 2023, **968**, 171694.

82 M. Yu, X. Li, Y. Ma, R. Liu, J. Liu and S. Li, *Appl. Surf. Sci.*, 2017, **396**, 1816–1824.

83 X. Hong, H. You, C. Deng, G. Wang and W. Dong, *J. Alloys Compd.*, 2024, **1002**, 175239.

84 D. Malavekar, V. Magdum, S. Khot, J. Kim and C. Lokhande, *J. Alloys Compd.*, 2023, **960**, 170601.

85 W. Dong, H. You, C. Deng, G. Wang and X. Hong, *Ceram. Int.*, 2024, **50**, 25465–25472.

86 Y. Sun, S. Guo, W. Li, J. Pan, C. Fernandez, R. A. Senthil and X. Sun, *J. Power Sources*, 2018, **405**, 80–88.

87 Q. Fu, M. Yang, Z. Liu, H. Yang, F. She, X. Zhang, F. Xie, Y. Hu and J. Chen, *J. Colloid Interface Sci.*, 2022, **618**, 161–172.

88 P. Phonsuksawang, P. Khajondetchairit, K. Ngamchuea, T. Butburee, S. Sattayaporn, N. Chanlek, S. Suthirakun and T. Siritanon, *Electrochim. Acta*, 2021, **368**, 137634.

89 C. Yan, X. Yang, S. Lu, E. Han, G. Chen, Z. Zhang, H. Zhang and Y. He, *J. Alloys Compd.*, 2022, **928**, 167189.

90 C. Lu, Y. Zhang, M. Sun, P. Zou, X. Wang, Y. Wang, Q. Huang, H. Chen, J. Ye and H. Rao, *J. Power Sources*, 2021, **516**, 230685.

91 N. Nwaji, H. Kang, M. Goddati, L. T. Tufa, J. Gwak, A. Sharan, N. Singh and J. Lee, *J. Mater. Chem. A*, 2023, **11**, 3640–3652.

92 W. Cao, Y. Liu, F. Xu, Q. Xia, G. Du, Z. Fan and N. Chen, *Electrochim. Acta*, 2021, **385**, 138433.

93 F. Lai, J. Feng, T. Heil, Z. Tian, J. Schmidt, G.-C. Wang and M. Oschatz, *J. Mater. Chem. A*, 2019, **7**, 19342–19347.

94 Y. Feng, W. Liu, Y. Wang, W. Gao, J. Li, K. Liu, X. Wang and J. Jiang, *J. Power Sources*, 2020, **458**, 228005.

95 L. Kang, C. Huang, J. Zhang, M. Zhang, N. Zhang, S. Liu, Y. Ye, C. Luo, Z. Gong and C. Wang, *Chem. Eng. J.*, 2020, **390**, 124643.

96 C. Zhang, Z. Lin, C. Huang, B. Zheng, Y. Li, J. Wang, M. Deng, S. Tang and Y. Du, *ACS Appl. Energy Mater.*, 2019, **2**, 6599–6607.

97 S. Jia, J. Wei, B. Gong and Z. Shao, *J. Colloid Interface Sci.*, 2021, **601**, 640–649.

98 Y. Zhang, L. Ye, J. Guo, Y. Shang, F. Guo, Y. Zhang and J. Xu, *J. Mater. Sci.*, 2021, **56**, 9368–9381.

99 L. Hua, Z. Hui, Y. Sun, X. Zhao, H. Xu, Y. Gong, R. Chen, C. Yu, J. Zhou and G. Sun, *Nanoscale*, 2018, **10**, 21006–21012.

100 W. Zong, F. Lai, G. He, J. Feng, W. Wang, R. Lian, Y. E. Miao, G. C. Wang, I. P. Parkin and T. Liu, *Small*, 2018, **14**, 1801562.

101 C. Li, R. Jin, S. Ke, S. Liu, Q. Li, Q. Liu and Y. Zhang, *Electrochim. Acta*, 2024, **475**, 143594.

102 Y. Qu, L. Sun, F. Xie, J. Hu, H. Tan and Y. Zhang, *Appl. Surf. Sci.*, 2023, **623**, 157037.

103 X. Qian, Y. Yin, Y. Lu, J. Xia, B. Huang, J. Sun, G. He and H. Chen, *J. Alloys Compd.*, 2022, **913**, 165191.

104 C. Huang, A. Gao, F. Yi, Y. Wang, D. Shu, Y. Liang, Z. Zhu, J. Ling and J. Hao, *Chem. Eng. J.*, 2021, **419**, 129643.

105 Z. Cui, W. Zheng, T. Meng, L. Lin, L. Yang, J. Zhong, W. Fan, Y. Tong and D. Shu, *Energy Storage Mater.*, 2024, **71**, 103681.

106 W. Shao, Q. Wang and D. Zhang, *J. Colloid Interface Sci.*, 2022, **617**, 84–93.

107 J. Tian, H. Guo, M. Wang, Y. Hao, J. Xu, H. Ren, Y. Hui and W. Yang, *J. Alloys Compd.*, 2024, **985**, 173949.

108 D. Zhang, S. Gao, J. Zhang, J. Wang, W. She, K. Wang, X. Xia, B. Yang and X. Meng, *J. Power Sources*, 2021, **514**, 230590.

109 Y.-M. Fan, Y. Liu, X. Liu, Y. Liu and L.-Z. Fan, *Electrochim. Acta*, 2017, **249**, 1–8.

110 A. M. Zardkhoshoui, B. Ameri and S. S. H. Davarani, *Nanoscale*, 2021, **13**, 2931–2945.

111 A. M. Zardkhoshoui and S. S. H. Davarani, *Nanoscale*, 2020, **12**, 12476–12489.

112 J. Li, J. Yang, P. Wang, Z. Cong, F. Shi, L. Wei, K. Wang and Y. Tong, *Int. J. Biol. Macromol.*, 2023, **232**, 123344.

113 Y. Liu, J. Zhou, W. Fu, P. Zhang, X. Pan and E. Xie, *Carbon*, 2017, **114**, 187–197.